Research Article J. Electrochem. Sci. Technol., 2021, 12(2), 246-256

Mo,Cu-doped CeO_2 as Anode Material of Solid Oxide Fuel Cells (SOFCs) using Syngas as Fuel

Isaac Díaz-Aburto[1,2], Jacqueline Hidalgo[1,3], Eliana Fuentes-Mendoza[1,3], Sergio González-Poggini[1,3], Humberto Estay[1], and Melanie Colet-Lagrille[1,3]*

[1]*Advanced Mining Technology Center (AMTC), Faculty of Physical and Mathematical Sciences, Universidad de Chile, Av. Tupper 2007 (AMTC Building), Santiago, Chile*

[2]*Department of Chemistry, Faculty of Natural Sciences, Mathematics and Environment, Universidad Tecnológica Metropolitana, Las Palmeras 3360, Ñuñoa, Santiago, Chile*

[3]*Department of Chemical Engineering, Biotechnology and Materials, Faculty of Physical and Mathematical Sciences, Universidad de Chile, Beauchef 851, Santiago, Chile*

ABSTRACT

Mo,Cu-doped CeO_2 (CMCuO) nanopowders were synthesized by the nitrate-fuel combustion method aiming to improve the electrical and electrochemical properties of its Mo-doped CeO_2 (CMO) parent by the addition of copper. An electrical conductivity of ca. $1.22 \cdot 10^{-2}$ S cm^{-1} was measured in air at 800°C for CMCuO, which is nearly 10 times higher than that reported for CMO. This increase was associated with the inclusion of copper into the crystal lattice of ceria and the presence of Cu and Cu_2O as secondary phases in the CMCuO structure, which also could explain the increase in the charge transfer activities of the CMCuO based anode for the hydrogen and carbon monoxide electro-oxidation processes compared to the CMO based anode. A maximum power density of ca. 120 mW cm^{-2} was measured using a CMCuO based anode in a solid oxide fuel cell (SOFC) with YSZ electrolyte and LSM-YSZ cathode operating at 800°C with humidified syngas as fuel, which is comparable to the power output reported for other SOFCs with anodes containing copper. An increase in the area specific resistance of the SOFC was observed after ca. 10 hours of operation under cycling open circuit voltage and polarization conditions, which was attributed to the anode delamination caused by the reduction of the Cu_2O secondary phase contained in its microstructure. Therefore, the addition of a more electroactive phase for hydrogen oxidation is suggested to confer long-term stability to the CMCuO based anode.

Keywords : SOFC Anode Material, Ceria, Molybdenum Oxide, Copper Nanoparticles, Syngas Fuel

Received : 19 October 2020, Accepted : 18 December 2020

1. Introduction

Solid oxide fuel cells (SOFCs) are considered a promising technology for power generation due to their high chemical to electrical energy conversion efficiency and minimum greenhouse gas emissions produced during operation. Ni-YSZ composites (cermets) are the most widely used anode materials in SOFCs since they present excellent catalytic activity and long-term stability for the electrochemical oxidation of hydrogen. However, the performance of Ni-YSZ anodes shows degradation when carbonaceous fuels – such as methane or syngas – are used as an alternative to hydrogen, which is not yet a readily available fuel. This degradation is related to the formation of stable carbon deposits on the surface of the electrode catalyzed by nickel and sulfur poisoning of this metal, which block and deactivate the anode triple phase boundaries (TPBs) [1-4].

In this context, cerium dioxide or ceria (CeO_2) has emerged as a promising anode material for SOFCs using carbonaceous fuels instead of hydrogen, owing to its high resistance to carbon deposition and sulfur poisoning during the processes of reformation and electro-oxidation of methane and syngas [5,6]. However, the electrical conductivity of CeO_2 needs to be

*E-mail address: mcolet@ing.uchile.cl

DOI: https://doi.org/10.33961/jecst.2020.01571

increased – preferably by means of doping with cost-effective accessible transition metals – to circumvent undesirable high ohmic losses during SOFCs operation. Recently, Mo-doped CeO_2 has been reported as a stable ceria-based anode material with higher catalytic activity for carbon gasification and electrical conductivity than pure CeO_2 (a value of ca. $1.87 \cdot 10^{-3}$ S cm^{-1} at 800°C was measured under air atmosphere for Mo-doped CeO_2 with 10 wt.% Mo), although this latter needs to be at least one order of magnitude larger for SOFC applications [7].

The addition of copper to CeO_2-based anodes has been studied in order to increase the electrical conductivity of these ceramic composites for their application in SOFCs using carbonaceous fuels, considering that Cu also shows high resistance to carbon deposition [5,6,8-12]. Nevertheless, the fabrication of Cu-containing CeO_2 anodes cannot be accomplished by simple mixing of Cu_2O or CuO with CeO_2 followed by sintering, since CuO reacts to form Cu_2O over ca. 700°C and the melting point of Cu_2O is ca. 1150°C which is lower than the temperature required for sintering CeO_2 under atmospheric oxygen pressure [13]. In addition, CuO can react at the interface with the YSZ electrolyte at high temperatures, promoting the formation of a monoclinic ZrO_2 phase [14,15]. Impregnation methods have been employed for the fabrication of Cu-doped anodes in order to overcome the limitations previously stated, though a large number of impregnation and subsequent calcination steps are required to reach a significant metal load in the electrode structure which, in addition, is heterogeneously distributed [16,17].

In this work, copper was added effectively into the microstructure of recently reported Mo-doped CeO_2 to improve its electrical and electrochemical properties by synthesizing Mo,Cu-doped CeO_2 via a simple nitrate-fuel combustion route. The characterization of the Mo,Cu-doped CeO_2 nanopowders synthesized is presented, and compared with its Mo-doped CeO_2 parent, together with an analysis of the electrical conductivity of this material under air atmosphere. Additionally, the performance of a SOFC with Mo,Cu-doped CeO_2-based anode using syngas as fuel is discussed in the light of polarization and power density curves, electrochemical impedance spectroscopy analysis and a characterization of the SOFC components after operation.

2. Experimental

2.1 Synthesis and characterization of Mo,Cu-doped CeO_2 nanopowders

Mo,Cu-doped CeO_2 (CMCuO) nanopowders were synthesized by the nitrate-fuel combustion method based on the procedure reported elsewhere for the synthesis of Mo-doped CeO_2 nanopowders [7]. Reagents used were citric acid ($C_6H_8O_7$, Sigma-Aldrich, 99.5% purity), as organic fuel and chelating agent, along with cerium nitrate ($Ce(NO_3)_3 \cdot 6H_2O$, Sigma-Aldrich, 99% purity), ammonium molybdate ($(NH_4)_6Mo_7O_{24} \cdot 4H_2O$, Merck, 99% purity) and copper nanoparticles (Cu, Sigma-Aldrich, 25 nm size), as metal oxide precursors. For the synthesis of CMCuO nanoparticles with 5 wt.% of molybdenum and 5 wt.% of copper content, 1.0 M cerium nitrate (10 mL), 1.0 M citric acid (10 mL) and 0.016 M ammonium molybdate (10 mL) solutions were prepared. The cerium nitrate and citric acid solutions were mixed and stirred for 20 minutes at room temperature, followed by the addition of the ammonium molybdate solution and stirring for other 20 minutes. Finally, 0.31 g of copper nanoparticles were added to the mixture followed by stirring for 10 minutes more. The solution obtained was filtered and heated up to 500°C (in air) for 10 minutes in a Brasimet K-400 box furnace, to obtain a porous foam which was grinded in a mortar and calcined at 650°C for 2 hours (heating and cooling rates of 5°C min^{-1}) to produce the fully-crystalline CMCuO nanopowders.

It is worth to note that a composition of 5 wt.% of molybdenum and 5 wt.% of copper was selected after a thorough experimental procedure since higher values of these components, e.g., 10 wt.% of molybdenum and 10 wt.% of copper, promoted the evident formation of an undesirable molybdenum oxide secondary phase.

The shape, size and crystallinity of the calcined CMCuO nanoparticles were characterized by transmission electron microscopy (TEM) coupled with selected area electron diffraction (SAED) using a Hitachi Model HT7700 microscope. Their crystalline structure and the presence of secondary phases in the samples were studied by SAED and X-ray diffraction (XRD) using a Bruker D8 Advanced diffractometer. Finally, a thermal stability analysis of the calcined CMCuO nanoparticles was accomplished by thermogravimetric analysis (TGA) in nitrogen and air

atmospheres using a NETZSCH TG 209 F1 Libra analyzer, in the temperature range between 25 and 950ºC (heating rate of 20ºC min^{-1}).

2.2 CMCuO electrical conductivity measurements

The electrical conductivity of CMCuO was measured by the four-probe method using CMCuO dense pellets of ca. 12 mm of diameter and ca. 1 mm of thickness produced by uni-axial compression (pressure applied of ca. 100 MPa) of calcined CMCuO nanopowders. The green pellets obtained were sintered in air at 1000ºC for 24 hours in a Nabertherm LHTCT 01/16 box furnace, using heating and cooling rates of 1ºC min^{-1}. The sintered pellets were polished with sandpaper and exposed to a thermal etching process at 950ºC for 1 hour using heating and cooling rates of 5ºC min^{-1}, to reduce residual stress in the final product.

The sintering temperature selected to obtain dense CMCuO pellets corresponds to the maximum one at which the material can be exposed without affecting its structure/composition (stability limit). Thermal etching conditions were select after a thorough experimental procedure.

The electrical conductivity measurements were performed under ultra-pure air atmosphere (100 mL min^{-1} flow rate) and the results obtained were compared with the data reported in the literature for pure CeO_2 (ceria) and Mo-doped CeO_2 with 10 wt.% molybdenum content (CMO10) [7]. The electrical connections were made with 4 spots of silver paste (Fuel Cells Materials) and silver wires (99.99% metal basis and 0.5 mm of diameter), connecting the silver wires with the surface of the sintered disc. Silver paste was dried at 100ºC for 1 hour and then cured at 800ºC for 1 hour using heating and cooling rates of 1ºC min^{-1}. The sintered disc was heated to the desired temperature in the range of 500-800ºC using a tubular furnace with PID controller. A Gamry Reference 3000 potentiostat/galvanostat/ZRA was used to determine the electrical conductivity of the material through cyclic voltammetry measurements at each temperature. The data obtained was fitted using the van der Pauw equation and the conductivity values were obtained for each temperature [18].

2.3 Fabrication of solid oxide fuel cells and experimental test rig

Commercial 8-YSZ electrolyte discs of 20 mm of diameter and 0.25 mm of thickness (Fuel Cell Materials) were used as cell support. The cathode was coated in one side of the electrolyte disc by spin-coating (1500 rpm), using commercial LSM-YSZ and LSM pastes (Fuel Cell Materials). Two layers of circular section (1.54 cm^2) were coated with each paste, all of them dried at 50ºC for 30 minutes in a hot plate before applying the next one, and finally sintered in a Nabertherm LHTCT 01/16 box furnace at 1100ºC for 3 hours. For the anode fabrication, two pastes based on CMCuO were prepared. Firstly, the CMCuO nanoparticles synthesized were mixed and crushed in a mortar with GDC nanoparticles – which were synthesized following the procedure described in [19] - in a 1:1 weight ratio, and added to a commercial terpineol-based organic carrier (Fuel Cell Materials) in a 7:3 weight ratio to produce a mixed ionic-electronic conductor (MIEC) paste. Secondly, a pure CMCuO current collector paste was prepared mixing the synthesized nanoparticles with the organic carrier in a 7:3 weight ratio. Lastly, as for the cathode, two layers of circular section (1.54 cm^2) were painted with each paste in the clean side of the electrolyte disc by spin-coating (1500 rpm), all of them dried at 50ºC for 30 minutes in a hot plate before applying the next one, and finally sintered in a Nabertherm LHTCT 01/16 box furnace at 1100ºC for 3 hours (heating and cooling rates of 3ºC min^{-1}).

A mesh of platinum was paint-brushed on both sides of the fabricated cell, using platinum paste (Fuel Cell Materials), for current collection. The platinum paste was dried at 100ºC for 1 hour (heating rate of 3.5ºC min^{-1}) and sintered at 1100ºC for 4 hours (heating and cooling rates of 1ºC min^{-1}) in a Nabertherm LHTCT 01/16 box furnace. The SOFC fabricated was supported in an alumina tube with the anode facing the inside in intimate contact with a platinum mesh and wires, attached to the tube end using alumina-based cement (Ceramabond 552, Aremco) cured for 2 hours at room temperature. After curing, an alumina lid with a platinum mesh and wires attached was placed over the cathode side and fixed using alumina-based cement as well. Following another 2 hours of curing at room temperature, the alumina-based cement was subjected to a thermal treatment at 94ºC for 2 hours (heating rate of 3.5ºC min^{-1}) and 260ºC for 2 hours (heating and cooling rates of 3.5ºC min^{-1}) in a Nabertherm RD 30/200/13 tubular furnace. Finally, the alumina tube open

side was sealed with a stainless-steel cap connected to gas lines.

For comparison of the electro-oxidation charge transfer activities of CMCuO and its CMO10 parent, via electrochemical impedance spectroscopy under OCV conditions, a SOFC with CMO10-based anode was fabricated following an analogous methodology to this described above.

2.4 Electrochemical measurements

Electrochemical impedance spectroscopy (EIS) and linear sweep voltammetry tests were carried out to study the performance of the SOFC using humidified syngas as fuel. The electrochemical tests were performed in a Gamry Reference 3000 potentiostat/galvanostat/ZRA.

A flow of 100 mL min^{-1} of humidified syngas (3 vol.% $H_2O(g)$ – 48.5 vol.% $H_2(g)$ – 48.5 vol.% CO(g)) was fed to the anode; the cathode was fed with 100 mL min^{-1} of ultra-pure air, and the SOFC was placed inside a Nabertherm RD 30/200/13 tubular furnace during tests. Temperature was increased at a heating rate of 5°C min^{-1} up to 600°C for the first measurements. Open circuit voltage (OCV) of the fuel cell was measured for 1 hour to corroborate its stability.

EIS measurements were performed under OCV and polarization conditions at the cell voltage at which the maximum power density was obtained (ca. 0.6 V at 800°C). A perturbation signal with 10 mV AC amplitude was applied in both cases. Frequencies analyzed were between 300 kHz and 10 mHz, correspondingly with 10 points per decade. EIS measurements under OCV were performed between 600 and 800°C every 50°C at the gas flow conditions stated above, and at 800°C varying the fuel concentrations by diluting with argon (same flow rate). In addition, a total of 5 cycles of EIS measurements under OCV followed by EIS measurements under polarization conditions were carried out to study the variability of the SOFC total impedance (at 800°C and non-diluted fuel concentration conditions). After each polarization cycle, the system was left to rest for 30 minutes so that the OCV value reached stability.

Polarization curves were obtained by linear sweep voltammetry between 600 and 800°C every 50°C at non-diluted fuel concentration conditions, and at 800°C varying the fuel concentrations by diluting with argon (same to EIS measurements). The cell voltage was changed between the OCV value and 0 V at a scan rate of 15 mV s^{-1} with a step size of 1 mV.

2.5 SOFC characterization before and after electrochemical measurements

The morphology of the SOFC cross section before and after electrochemical tests was characterized by scanning electron microscopy (SEM) in a JEOL JSM-IT300LV. The crystalline structure of the anode surface before and after electrochemical tests was studied by XRD using a Bruker D8 Advance diffractometer.

3. Results and Discussion

3.1 CMCuO characterization and electrical conductivity

Fig. 1(a) shows a TEM micrograph of calcined CMCuO nanoparticles, which as a trend present an

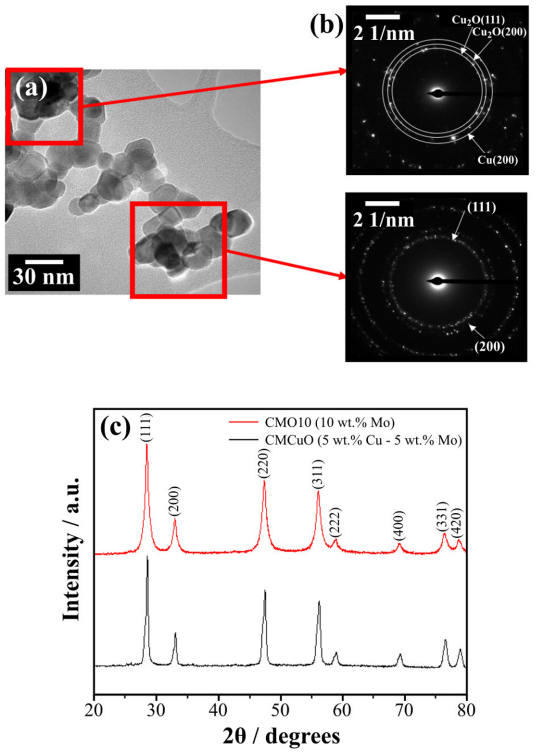

Fig. 1. (a) TEM micrograph of calcined CMCuO nanoparticles, (b) SAED patterns of calcined CMCuO nanoparticles and (c) XRD pattern of calcined CMCuO and CMO10 nanoparticles.

irregular spherical shape and an average size of 20 nm. Fig. 1(b) shows SAED patterns of these nanoparticles, which reveal the presence of secondary phases such as Cu_2O and Cu together with the main ceria-like structure with the more exposed crystal planes being (111) and (200). The XRD pattern of calcined CMCuO nanoparticles, which is shown in Fig. 1(c), indicates that CMCuO crystallizes as a Fm-3m fluorite-type structure, likewise its CMO10 parent [7]. The displacement of the peaks in the XRD pattern of CMCuO with respect to the peaks in the XRD pattern of CMO10, which is confirmed by the change in the lattice parameter calculated for CMCuO (5.424 Å) with respect to the lattice parameter of CMO10 (5.421 Å [7]), can be related to the inclusion of Cu into the crystalline structure of ceria. This would promote the formation of oxygen vacancies and add electrons in the Ce-sites in accordance with the reaction in Eq. (1) expressed in the Kröger-Vink notation [20]:

$$CuO \xrightarrow{CeO_2} Cu''_{Ce} + V_O^{\bullet\bullet} + O_O^x \qquad (1)$$

which can enhance the total electrical conductivity and electro-oxidation charge transfer activities of the anode material, as will be further discussed.

The thermal stability of calcined CMCuO nanoparticles was confirmed by TGA analysis in nitrogen and air atmospheres, which showed no significant changes in the mass of the samples.

The plots for the total electrical conductivity (σ) of pure ceria, CMO10 [7] and CMCuO under air atmosphere as a function of temperature are shown in Fig. 2(a). The total electrical conductivity of CMCuO presents values very similar to those reported for CMO10 and exhibits an Arrhenius-like behavior with good determination coefficient (see Fig. 2(b)) between 500 and 750ºC. However, a sharp increase of the total electrical conductivity of CMCuO occurs at 800ºC, which reaches a value of ca. $1.22 \cdot 10^{-2}$ S cm^{-1} while the values reported for pure ceria and CMO10 at this temperature are ca. $5.65 \cdot 10^{-4}$ S cm^{-1} and ca. $1.85 \cdot 10^{-3}$ S cm^{-1}, respectively. This change in the electrical conductivity behavior can be explained by: (i) the inclusion of copper into the crystalline structure of ceria and (ii) the presence of free Cu and Cu_2O – which becomes stable at 800ºC – as secondary phases in the CMCuO structure, both of which are good electrical conductors [13,21]. Therefore, the addition of copper enhances the electrical conductivity of the anode material with respect to its CMO10 parent at the SOFC operating temperature, as it was aimed.

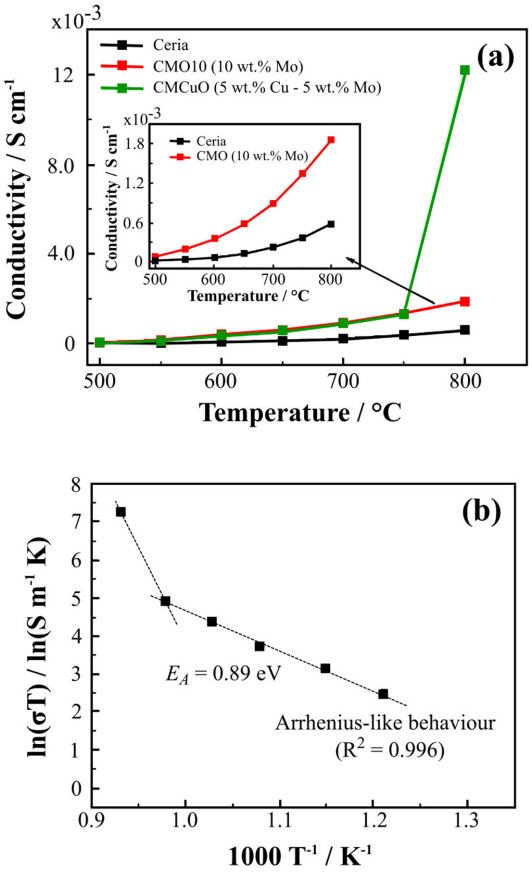

Fig. 2. (a) Conductivity measurements of pure ceria, CMO10 and CMCuO in pure air, (b) linear regression of the conductivity data for CMCuO shown in (a). The conductivity data for pure ceria and CMO10 corresponds to that reported by the authors in [7].

3.2 SOFC with CMCuO-based anode: H_2 and CO electro-oxidation charge transfer activities

Figs. 3(a) and 3(b) show the Nyquist plots associated with the EIS tests under OCV (1.04 V) conditions of a SOFC with CMCuO-based anode using humidified syngas as fuel at: (a) different temperatures and (b) different syngas concentrations (diluted in argon) at 800ºC. As can be seen in Fig. 3(a), at all temperatures a small semicircle (low impedances) is observable at high frequencies followed by a lobular-shaped sector associated with higher impedances at

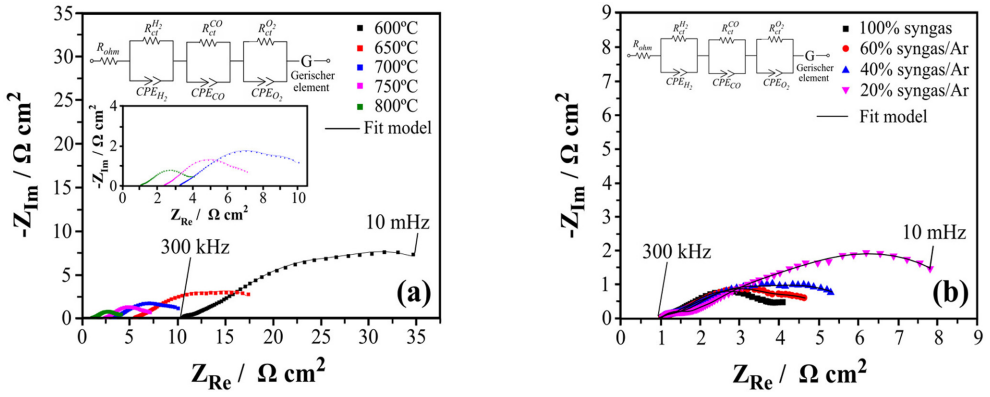

Fig. 3. Nyquist plots associated with the EIS tests under OCV conditions of a SOFC with CMCuO-based anode at: (a) different temperatures using pure humidified syngas as fuel and (b) different syngas concentrations and 800ºC. (It is worth to note that the data presented in this figure were Kramers-Kronig transformable).

intermediate and low frequencies. As expected, the higher the temperature the lower the total impedance due to the enhancement of the electrocatalytic and purely catalytic activities at the electrodes. Fig. 3(b) shows that a decrease in the fuel concentration at 800ºC promotes an increase of the total impedance at intermediate and low frequencies, which suggests that the lobular-shaped sectors of the Nyquist plots are related to the anodic charge transfer and reforming processes. On the contrary, no changes are observable for the low frequency semicircles which suggests that these are related to the cathodic charge transfer processes.

The equivalent circuit model presented in Figs. 3(a) and 3(b) was proposed to fit the EIS data. The R_{ohm} element represents the total SOFC ohmic losses (electrolyte, anode, cathode and current collectors resistances), while the three *R(CPE)* elements represent the H_2 and CO electro-oxidation and the O_2 electro-reduction processes at the anode and cathode, respectively (R_{ct}^{i}: electrodes charge transfer resistances and CPE_i: constant phase elements associated to the transport of oxide ions (O^{2-}) towards/from the TPBs). Finally, a Gerischer element was included to represent the catalytic reforming process of syngas taking place at the anode surface before electro-oxidation occurs [22,23]. The parameters associated to each element of the equivalent circuit model proposed were fitted using the Gamry Echem Analyst software v6.23 and exhibit a goodness of fit factor in the range of 10^{-5} – 10^{-6}. Tables 1 and 2 summarize the results obtained.

The charge transfer resistances, R_{ct}^{i}, obtained as a function of temperature using pure humidified syngas as fuel (Table 1) were fitted using an Arrhenius-like model to determine the activation energies (E_A^i) associated to each of them. Table 3 presents the results obtained as well as the corresponding coefficients of determination (R^2). The activation energy obtained for the oxygen electro-reduction reaction is

Table 1. Contact resistances obtained from the equivalent circuit model fitting of the EIS data at different temperatures (Fig. 3a).

Temperature (ºC)	R_{ohm} (Ω cm^2)	$R_{ct}^{H_2}$ (Ω cm^2)	R_{ct}^{CO} (Ω cm^2)	$R_{ct}^{O_2}$ (Ω cm^2)	$R_{Gerischer}$ (Ω cm^2)
600	10.44	3.91	12.47	3.54	9.52
650	5.44	2.09	4.84	2.14	4.89
700	3.23	0.81	2.62	1.22	3.69
750	2.37	0.61	1.23	0.63	2.33
800	1.13	0.22	0.39	0.45	1.09

Table 2. Contact resistances obtained from the equivalent circuit model fitting of the EIS data at different syngas concentrations (Fig. 3b).

Syngas concentration	R_{ohm} (Ω cm^2)	$R_{ct}^{H_2}$ (Ω cm^2)	R_{ct}^{CO} (Ω cm^2)	$R_{ct}^{O_2}$ (Ω cm^2)	$R_{Gerischer}$ (Ω cm^2)
100%	1.13	0.22	0.39	0.45	1.09
60%	1.12	2.18	0.80	0.47	0.85
40%	1.12	2.92	1.16	0.54	0.52
20%	1.14	3.98	3.05	0.49	0.86

Table 3. Activation energies associated with the charge transfer resistances (R_{ct}^{i}) in a SOFC with CMCuO-based anode using humidified syngas as fuel.

R_{ct}^{i}	E_A (eV)	R^2
$R_{ct}^{O_2}$	0.90	0.98
$R_{ct}^{H_2}$	1.12	0.98
R_{ct}^{CO}	1.33	0.99

in good agreement with the values reported in the literature for LSM-based cathodes [24,25]. The identification of the anodic charge transfer resistances obtained with the H_2 and CO electro-oxidation processes was accomplished considering that the first should present a lower activation energy compared to the second, as reported in [26]. The difference between the activation energies obtained for the hydrogen and carbon monoxide electro-oxidation processes is of ca. 19%, which suggests that the anode electrocatalytic activities for these reactions are comparable.

For comparison purposes, the activation energies associated with the hydrogen and carbon monoxide electro-oxidation processes were similarly obtained for a SOFC with CMO10-based anode using pure humidified syngas as fuel. The values obtained were 1.30 eV and 1.80 eV for hydrogen and carbon monoxide, respectively, which are ca. 16% and ca. 35% higher than these obtained for the SOFC with CMCuO-based anode. These results indicate that the addition of copper into the microstructure of CMO10 is not only beneficial for the electrical conductivity of the material (the total SOFC ohmic losses decrease from 2.51 Ω cm^2 to 1.13 Ω cm^2 at 800ºC when adding copper to the electrode), but also for its charge transfer activities. Therefore, CMCuO seems to be an adequate anode material for SOFC applications.

3.3 SOFC with CMCuO-based anode: Polarization and power density curves

To compare the energy generation capacity of a SOFC with CMCuO-based anode using humidified syngas as fuel with other analogous technologies, Figs. 4(a) and 4(b) show the polarization curves and power density curves obtained at: (a) different temperatures and (b) different syngas concentrations (diluted in argon) at 800ºC. The OCVs measured before polarization remained constant during the whole electrochemical experiments and varied linearly between ca. 1.04 V and 1.0 V when decreasing the temperature (Fig. 4(a)) and logarithmically between 1.04 and 0.84 V when decreasing the fuel concentration in the anode gas stream (Fig. 4(b)), which is in good agreement with the behavior predicted by the Nernst equation [27]. The maximum electrical power density measured for this system was ca. 120 mW cm^{-2} at a current density of ca. 200 mA cm^{-2} and a cell voltage of ca. 0.6 V when operating at 800ºC and non-diluted fuel concentration conditions. This result was expected considering that the higher the temperature and fuel concentration, the lower the ohmic losses and charge transfer resistances as shown in Tables 1 and 2.

Vohs *et al*. obtained the same electrical power density (ca. 120 mW cm^{-2}) operating at 700ºC using syngas as fuel in a SOFC with Cu-CeO_2-YSZ anode, YSZ electrolyte and LSF-YSZ cathode (support) [28]. Hill and Islam reported a maximum power density of ca. 49 mW cm^{-2} using dry methane as fuel in a SOFC with Cu-Ni/YSZ anode, YSZ electrolyte (support) and LSM-YSZ cathode operating at 800ºC [17]. Gorte *et al*. reported a maximum power density of ca. 330 mW cm^{-2} feeding methane as fuel in a SOFC with Cu-Ni-YSZ/CeO_2 anode (support), YSZ electro-

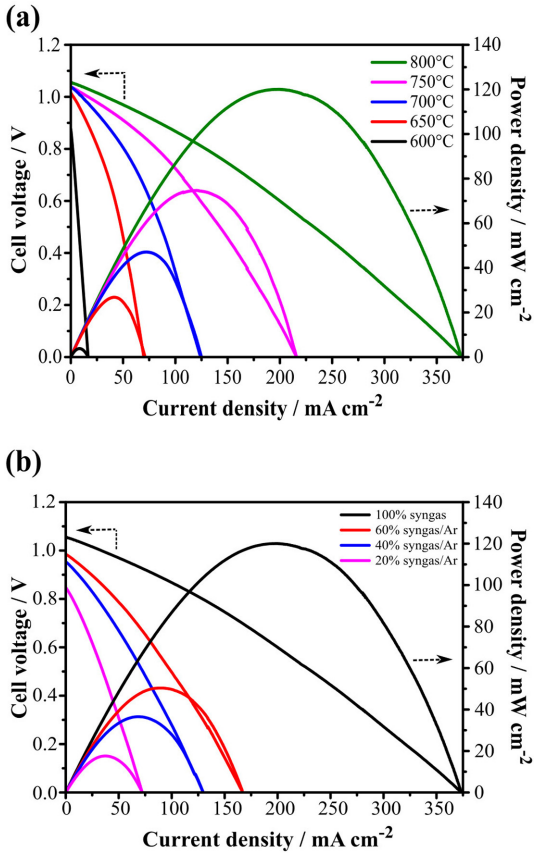

Fig. 4. Polarization (j-E: current density-voltage) curves and power density (j-P: current density-power density) curves of a SOFC with CMCuO-based anode at: (a) different temperatures using pure humidified syngas as fuel and (b) different syngas concentrations and 800°C.

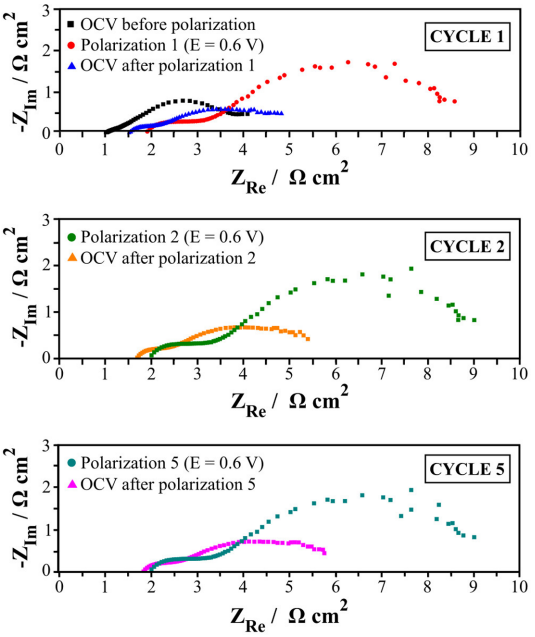

Fig. 5. Nyquist plots associated with EIS measurements under OCV conditions followed by EIS measurements under a cell voltage of 0.6 V for a SOFC with CMCuO-based anode at 800°C using non-diluted humidified syngas as fuel. After each polarization cycle, the system was left to rest for 30 minutes so that the OCV value reached stability.

lyte and LSM-YSZ cathode operating at 800ºC [29]. As can be seen, the results obtained in this work for a SOFC with CMCuO-based anode using humidified syngas as fuel are comparable with those reported in the literature for SOFCs with anodes containing copper. Even more, the SOFC with CMCuO-based anode shows a higher maximum power density than an analogous SOFC with Cu-Ni/YSZ anode supported on the electrolyte and is only surpassed by SOFCs supported on the anode or cathode, which can be explained by the lower ohmic losses associated with them (the YSZ electrolyte in this work contribute with ca. 70% of the total ohmic resistance measured by EIS). Therefore, CMCuO seems a promising anode material for SOFCs using carbonaceous fuels.

3.4 SOFC with CMCuO-based anode: Stability analysis

Fig. 5 shows three out of five cycles of Nyquist plots associated with EIS measurements under OCV conditions followed by EIS measurements under a cell voltage of 0.6 V (polarization condition at the maximum power density, as stated in section 3.3) for a SOFC with CMCuO-based anode at 800ºC using non-diluted humidified syngas as fuel. After polarization, scattered points are observable at low frequencies under OCV conditions, which could be related to changes in the CMCuO-based anode microstructure (as explained at the end of this section) and thus the advent of diffusional limitations. The total area specific resistance (ASR) and the total SOFC ohmic losses (R_{ohm}) were calculated under OCV conditions before polarization and after each polarization cycle to obtain the values reported in Table 4. As can be seen, the ASR value obtained before polarization is 1.25 Ω cm^2 (ca. 23%) lower

Table 4. Total area specific resistance (ASR) and total ohmic losses (R_{ohm}) of a SOFC with CMCuO-based anode using humidified syngas as fuel operating at 800°C under OCV or polarization conditions at five EIS cycles.

Cycle	at OCV before polarization		under polarization at 0.6 V		at OCV after polarization	
	ASR (Ω cm^2)	R_{ohm} (Ω cm^2)	ASR (Ω cm^2)	R_{ohm} (Ω cm^2)	ASR (Ω cm^2)	R_{ohm} (Ω cm^2)
1	4.25	1.13	9.00	1.82	5.5	1.50
2	---	---	9.51	2.03	5.7	1.65
3	---	---	9.50	2.03	5.6	1.67
4	---	---	9.52	2.04	5.7	1.72
5	---	---	9.52	2.05	5.8	1.75

than the ASR value obtained after the first polarization cycle, while R_{ohm} before polarization is 0.37 Ω cm^2 (ca. 25%) lower than R_{ohm} after the first polarization cycle. Nevertheless, the changes in the ASR and R_{ohm} values in the following polarization cycles are not considerable compared to the ASR and R_{ohm} values measured after the first polarization cycle (maximum differences of 0.3 Ω cm^2 and 0.25 Ω cm^2, respectively). These results could be explained by changes observed in the CMCuO-based anode microstructure after ca. 10 hours of electrochemical tests, which are further discussed below.

The ASR value measured under polarization conditions is around 9 and 9.5 Ω cm^2 for the five cycles, while the Nyquist plots show a slight displacement to higher impedance values in the real axis at low frequencies. This also could be related to degradation of the CMCuO-based anode as diffusional impedances increase.

Fig. 6(a) shows the XRD analyses of the CMCuO anode surface before and after the electrochemical tests discussed in sections 3.2 to 3.4. As can be seen, two crystalline structures can be identified: the F phase (stronger signal) corresponding to the Fm-3m fluorite-type structure associated with the CMCuO-GDC composite and the 8-YSZ phase (weaker signal) associated with the supporting electrolyte. The presence of additional secondary crystalline phases is not noticeable in the diffractograms, apart from a platinum signal for the CMCuO anode surface after the electrochemical tests which corresponds to the current collector. These results suggest that the composition of the CMCuO-based anodes is relatively stable under operating conditions; however, long-term experiments need to be carried out to confirm this once the catalytic and electro-catalytic activity of the material is improved.

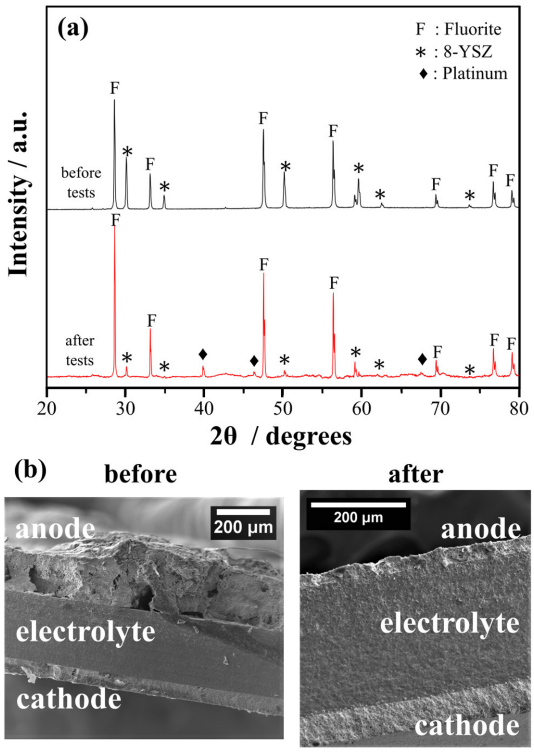

Fig. 6. (a) XRD analyses of the CMCuO anode surface before and after electrochemical tests, (b) SEM micrograph of the SOFC cross-section before and after electrochemical tests.

Fig. 6(b) shows the SEM analyses of the SOFC cross-section before and after the electrochemical tests. As can be seen, the SOFC electrodes before the electrochemical tests show good adhesion to the electrolyte and no signs of delamination. The electrodes and electrolyte thicknesses before the electrochemical tests are reported in Table 5. After the electrochemical tests the CMCuO-based anode exhibits a

Table 5. Average thicknesses of the fabricated SOFC electrodes and electrolyte (before electrochemical tests).

SOFC component	Thickness (μm)
Anode	165 ± 5
Electrolyte	250 ± 2
Cathode	53 ± 2

considerable decrease in its thickness (it goes from 165 ± 5 μm to 28 ± 5 μm), which suggests it delaminates during the SOFC operation probably due to shrinkage caused by the reduction of the Cu_2O secondary phase detected by SAED in the CMCuO structure (see section 3.1). This would affect seriously the long-term stability of the solid oxide fuel cell since an important amount of anode material is lost (particularly electronically conductive copper due to shrinkage) affecting the structure and continuity of the triple phase boundaries and, therefore, increasing the ASR and R_{ohm} values, as observed by other authors for different cermet anodes [30,31]. Thus, alternatives to protect the anode material against undesirable reduction during operation will have to be considered in future work. No changes are observable in the cathode thickness after the electrochemical tests.

4. Conclusions

Mo,Cu-doped CeO_2 was tested as anode material of a solid oxide fuel cell with YSZ electrolyte (support) and LSM-YSZ cathode operating at different temperatures and using humidified syngas as fuel. The polarization and power density curves obtained indicate that a maximum power density of ca. 120 mW cm^{-2} at a current density of ca. 200 mA cm^{-2} and a cell voltage of ca. 0.6 V can be produced by this electrochemical system at 800ºC and non-diluted fuel conditions, which is comparable with the power output reported for other solid oxide fuel cells with anodes containing copper. However, after ca. 10 hours of operation under cycling open circuit voltage (1.04 V) and maximum power density polarization conditions, an increase in the total area specific resistance and the total ohmic losses of the solid oxide fuel cell is observed. This could be attributed to the reduction of the Cu_2O secondary phase contained in the Mo,Cu-doped CeO_2 structure during operation which causes anode delamination and implies a serious impact in the long-term stability of the solid oxide fuel cell.

Based on the results obtained, it is suggested the modification of the Mo,Cu-doped CeO_2-based anode by mixing it with a more electroactive phase for the oxidation of hydrogen (such as nickel), so that reduction of the Cu_2O secondary phase is prevented and the total electrical conductivity and charge transfer activities of the material are not adversely affected. On the other hand, it is expected that the good catalytic activity of the ceria-based materials for the oxidation of carbonaceous fuels would act as a protection for the carbon deposition at the nickel surface, thus establishing a symbiotic relationship between both materials.

Acknowledgments

The authors thank Project Anillo en Ciencias y Tecnología Tópicos Minería ACM170003 and CONICYT-PIA Project AFB180004 for the financial support to this research. In addition, the authors thank Prof. Ali Akbari-Fakhrabadi from Department of Mechanical Engineering, Universidad de Chile, for providing the GDC powders used for the fabrication of the solid oxide fuel cells tested in this work.

References

[1] S. A. Saadabadi, A. Thallam Thattai, L. Fan, R. E. F. Lindeboom, H. Spanjers, P.V. Aravind, *Renew. Energy.*, **2019**, *134*, 194-214.
[2] F. S da Silva, T. M. de Souza, *Int. J. Hydrogen Energy.*, **2017**, *42(41)*, 26020-26036.
[3] K. Al-Khori, Y. Bicer, M. Koç, *J. Clean. Prod.*, **2020**, *245*, 118924.
[4] U. M. Damo, M. L. Ferrari, A. Turan, A. F. Massardo, *Energy*, **2019**, *168*, 235-246.
[5] I. Sreedhar, B. Agarwal, P. Goyal, S. A. Singh, *J. Electroanal. Chem.*, **2019**, *848*, 113315.
[6] N. Mahato, A. Banerjee, A. Gupta, S. Omar, K. Balani, *Prog. Mater. Sci.*, **2015**, *72*, 141-337.
[7] I. Díaz-Aburto, F. Gracia, M. Colet-Lagrille, *Fuel Cells*, **2019**, *19(2)*, 147-159.
[8] S. An, C. Lu, W. L. Worrell, R. J. Gorte, J. M. Vohs, *Solid State Ion.*, **2004**, *175(1-4)*, 135-138.
[9] B. J. M. Sarruf, J. E. Hong, R. Steinberger-Wilckens, P. E. V. de Miranda, *Int. J. Hydrogen Energy.*, **2020**, *45(8)*, 5297-5308.
[10] X. F. Ye, S. R. Wang, J. Zhou, F. R. Zeng, H. W. Nie, T. L. Wen, *J. Power Sources.*, **2011**, *196(13)*, 5499-5502.

[11] S. Wang, M. Zheng, M. Li, X. Wu, C. Xia, *J. Mater. Chem. A.*, **2016**, *4(15)*, 5745-5754.
[12] A. Hornés, G. Munuera, A. Fuerte, M. J. Escudero, L. Daza, A. Martínez-Arias, *J. Power Sources*, **2011**, *196(9)*, 4218-4225.
[13] R. D. Schmidt-Whitley, M. Martinez-Clemente, A. Revcolevschi, *J. Cryst. Growth.*, **1974**, *23(2)*, 113-120.
[14] S. J. Skinner, M. A. Laguna-Bercero, *Advanced Inorganic Materials for Solid Oxide Fuel Cells*., **2011**, 33-94.
[15] H. He, J. M. Vohs, R. J. Gorte, *J. Electrochem. Soc.*, **2003**, *150(11)*, A1470.
[16] W. Li, B. Guan, M. Liu, B. Wei, X. Zhu, Z. Wang, Z. Lü, *J. Solid State Electrochem.*, **2018**, *22(6)*, 1735-1743.
[17] S. Islam, J. M. Hill, *J. Power Sources.*, **2011**, *196(11)*, 5091-5094.
[18] L. J. van der Pauw, *Philips Res. Reports.*, **1958**, 13(1), 1-9.
[19] M. Jamshidijam, R. V. Mangalaraja, A. Akbari-Fakhrabadi, S. Ananthakumar, S. H. Chan, *Powder Technol.*, **2014**, *253*, 304-310.
[20] K. Kumar, N. K. Singh, H. S. Park, O. Parkash, *RSC Adv.*, **2016**, *6(55)*, 49883-49890.
[21] A. P. Young, C. M. Schwartz, *J. Phys. Chem. Solids.*, **1969**, *30(2)*, 249-252.
[22] A. Kromp, H. Geisler, A. Weber, E. Ivers-Tiffée, *Electrochim. Acta.*, **2013**, *106*, 418-424.
[23] R. Barfod, M. Mogensen, T. Klemensø, A. Hagen, Y. L. Liu, P. Vang Hendriksen, *J. Electrochem. Soc.*, **2007**, *154(4)*, B371.
[24] J. W. Erning, T. Hauber, U. Stimming, K. Wippermann, *J. Power Sources.*, **1996**, *61(1-2)*, 205-211.
[25] E. Siebert, A. Hammouche, M. Kleitz, *Electrochim. Acta.*, **1995**, *40(11)*, 1741-1753.
[26] K. M. Ong, W. Y. Lee, J. Hanna, A. F. Ghoniem, *Int. J. Hydrogen Energy.*, **2016**, *41(21)*, 9035-9047.
[27] V. M. Janardhanan, O. Deutschmann, *Z. Phys. Chem.*, **2007**, *221(4)*, 443-478.
[28] O. Costa-Nunes, R. J. Gorte, J. M. Vohs, *J. Power Sources*, **2005**, *141(2)*, 241-249.
[29] H. Kim, C. Lu, W. L. Worrell, J. M. Vohs, R. J. Gorte, *J. Electrochem. Soc.*, **2002**, *149(3)*, A247.
[30] T. Klemenso, C. C. Appel, M. Mogensen, *Electrochem. Solid-State Lett.*, **2006**, *9(9)*, A403-A407.
[31] H. Yokokawa, H. Tu, B. Iwanschitz, A. Mai, *J. Power Sources*, **2008**, *182(2)*, 400-412.